# 3-D Tunnel TiO_2 Crystal Phase as a Fast Charging Lithium Battery Anode from Stochastic Surface Walking-Based Material Screening

Ya-Hui Fang,[*,†] Si-Cong Ma,[‡] and Zhi-Pan Liu[*,‡]

†School of Chemical and Environmental Engineering, Shanghai Institute of Technology, Shanghai 201418, China

‡Collaborative Innovation Center of Chemistry for Energy Material, Shanghai Key Laboratory of Molecular Catalysis and Innovative Materials, Key Laboratory of Computational Physical Science (Ministry of Education), Department of Chemistry, Fudan University, Shanghai 200433, China

S *Supporting Information*

ABSTRACT: To search for both high-rate capacity and high stability Li-ion battery anodes, here we design a new strategy of high-throughput material screening based on novel global potential energy surface exploration techniques. This permits us to quantify the structural evolution thermodynamics for 11 candidate materials after lithiation. When reaching the high capacity (∼300 mA h/g) in lithiation, all bulk materials studied are shown to experience solid-to-solid phase transition with appreciable volume expansion. Among 11 candidates, we screen out a new three-dimensional (3-D) tunnel TiO_2 (TiO_2-S) phase to be a high-performance anode material. This TiO_2-S phase has a spinel-like structure, achieving only 5.5% volume expansion at 335.5 mA h/g capacity (Li + TiO_2 → $LiTiO_2$) and also possessing a fast charging kinetics as seen from the low Li diffusion barrier in a wide range of Li concentrations. Because all common stable forms of materials are not good anode materials at high-rate condition, our results indicate that metastable phases with 3-D open structures could be the choice for the next-generation Li-ion battery anode. A natural database for these candidates could be the delithiated crystal phases with open skeletons that are stable enough to survive in subsequent (dis)charging cycles.
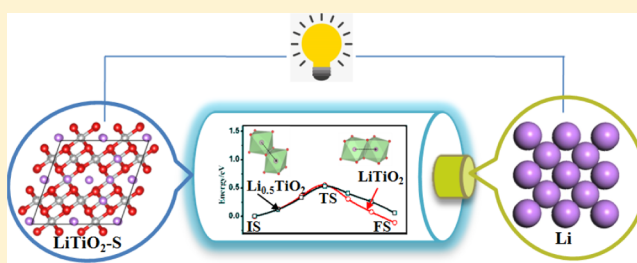
1. INTRODUCTION

Recent rapid developments in mobile electronic devices as well as electric vehicles demand better Li-ion batteries with high capacity, high-rate performance, and high stability.[1−6] The anode material is a major bottleneck for achieving the high performance considering that the common graphite cells suffer from low energy density (the engineering limit for the gravimetric capacity C_g is 372 mA h/g at LiC_6) and low charging speed (the reversible capacity is ∼370 mA h/g at the cycling current rate ∼C/24).[7] While huge efforts have been made to search for better Li-ion anode materials, such as Li−M (M = Si, Ge, Sn, etc.) alloys[8,9] and lithium transition-metal oxide (i.e., TiO_2),[10,11] it is common to note that the charging to high capacities is often accompanied with massive volume expansion that destroys the structural integrity of the material, which involves complex solid reactions and phase transitions. This structural variation results in electrode pulverization, capacity fading, and limited cycling life as well as safety issues.[12−14] A key in designing reliable Li-ion battery anodes in fast charging is thus to identify the controlling factors that influence the structural integrity of the material, which requires a detailed knowledge on the mechanism of structural evolution during lithiation.

The structural deformation in lithiation is undesirable because solid-to-solid reactions are generally slow and inelastic (irreversible). Unfortunately, the volume expansion and the corresponding structural deformation have been commonly observed on most anode materials, especially at high capacity. For a traditional graphite anode, it is ∼10% volume expansion at its capacity limit of LiC_6 (higher capacities are thermodynamically prohibited).[15] For the alloy anodes (Li_xM), although they can exhibit remarkable ability to host Li (i.e., 4200 mA h/g for $Li_{4.4}Si$, 1600 mA h/g for $Li_{4.4}Ge$, and 900 mA h/g for $Li_{4.4}Sn$) in theory, a massive volume expansion (>300%) and the crystal-to-amorphous phase transition can occur even in the first lithiation cycle at room temperature.[16,17] Advanced in situ techniques (e.g., X-ray diffraction and transmission electron microscopy) have confirmed the formation of solid solution Li_xSi at the high capacities, as expected from thermodynamics,[18,19] which is responsible for the large volume expansion compared to that of Si.

TiO_2 as an alternative material has received more attention because of its small volume expansion, better cyclability, and fast kinetics. Previous research[20−23] shows that (i) the maximum theoretical capacity, ∼335 mA h/g ($LiTiO_2$), can indeed be reached in specific samples, for example, <10 nm nanostructures for anatase.[24] (ii) The higher current rate is observed only at the relatively low capacity $Li_{x(x≤0.5)}TiO_2$ (e.g.,

~100 mA h/g at 30 C for anatase[25,26]). It was speculated that Li diffusion is kinetically restricted at the high Li intercalation condition, which should be affected by the lithium bonding environment in the TiO_2 lattice.[21,27] (iii) a number of Li_xTiO_2 polymorphs (i.e., anatase,[24,28] spinel,[29] and ramsdellite[30]) have been synthesized via different methods in the experiment. From theoretical calculations,[21] anatase $LiTiO_2$ is found to be the most stable among eight possible polymorphs of $LiTiO_2$ (rutile, anatase, brookite, TiO_2–B, ramsdellite, hollandite, spinel, and hexagonal). However, whether there are new TiO_2 phases with high performance in the Li-ion battery remains unknown.

Obviously, the lithiation-induced material degradation is a complex phenomenon influenced by many factors, for example, morphology, electronic structures (e.g., cohesive energy), and charging conditions (dynamics). The search for simple and robust parameters for the design of the better Li-ion battery represents a huge challenge to the field. In fact, the major problem in materials design is that the properties (volume, capacity, and stability) of the lithiated product Li_nX ($X + nLi^+ + ne^- \rightarrow Li_nX$) are generally unknown a priori because of the lack of knowledge on the atomic structure and chemical composition. It would be desirable to establish a high-throughput method to achieve the material screening. However, because of the slow kinetics of solid reactions, the traditional simulation tools, for example, molecular dynamics, have been frustrated for studying solid systems involving phase transitions because of the limited time scale in simulation. New theoretical tools are thus called for, which need to explore efficiently the likely lithiated solid phases and establish the global potential energy surface (PES). With the atomic structures of the thermodynamically stable lithiated product Li_nX, one would expect that the search for high-performance anode materials can be accelerated significantly.

2. METHODS

Here, we propose a three-step screening strategy to identify a better Li-ion anode material as shown in Scheme 1, namely,

Scheme 1. Three-Step Screening Strategy (Coarse Screening, Fine Screening, and Property Assessment) To Identify Better Li-Ion Anode Materials[a]
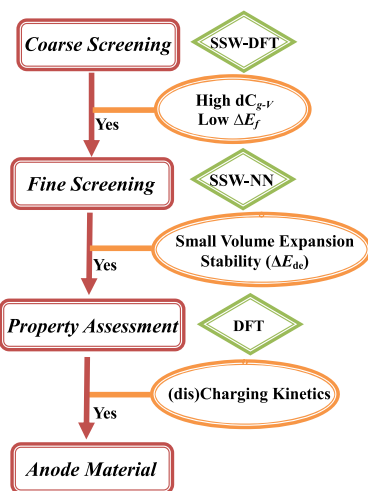
[a]SSW–DFT: first-principles-based SSW Global optimization. SSW–NN: SSW Global optimization using NN potential.

coarse screening, fine screening, and property assessment. Our method starts with a coarse screening step using the first principles-based stochastic surface walking (SSW) global optimization method [SSW-density functional theory (DFT)][31–33] to select potential candidates. The SSW global optimization has demonstrated the power in exploring solid phases and quantifying the phase transition kinetics.[34,35] This allows us to follow the complex solid phase transition trajectory in a high-throughput manner. We then utilize the fine screening procedure to focus on the promising candidates (e.g., $LiTiO_2$) using the latest machine-learning approach as implemented in the LASP code, that is, SSW–NN method[36–40] that combines the global neural network (NN) potential with the SSW method to explore the desirable composition (Li_xTiO_2 at different x ratios).With SSW–NN global search, one can routinely search for 10^7 structures on global PES for systems up to 100 atoms per cell and cover all likely compositions. At the final stage, the property assessment is utilized to evaluate the anode performance. The detail of the method and the calculation setup can be found in the Supporting Information. It should be mentioned that first-principles DFT calculations have been utilized to validate the low energy structures and confirm the identified global minimum (see the Supporting Information for details on DFT calculations). All energetics reported here are from DFT without specifically mentioning.

3. RESULTS

3.1. Coarse Screening. Our first-stage coarse screening is carried out as follows. We have explored the PES of lithiated materials with the Li/X ratio = 1 for 11 candidates with X being C (graphite), Si (cubic), Ag (fcc), Al (fcc), As (trigonal), Ge (cubic), Zn (cubic), Au (fcc), Sn (cubic), SnO_2 (tetragonal), and TiO_2 (anatase). The starting phase/structure of X in SSW exploration is indicated in parenthesis, which is utilized as the energy reference for pure material. The specific Li/X = 1 ratio is selected for two reasons: (i) it can yield the capacity above 300 mA h/g in general, the limiting capacity of graphite, which is naturally set as the minimum target to achieve and (ii) the simulation with this ratio can be carried out in relatively small supercells in periodic calculations, which can significantly expedite the PES exploration. It should be emphasized that the first-stage coarse screening is not aimed for finding the exact global minimum nor exploring exhaustively the PES of the target material but for selecting the potential candidates with good structure integrity. It is thus achievable within a reasonable short time even with first-principles-based SSW global optimization (e.g., using relatively small unit cells).

To analyze the large dataset obtained from SSW global optimization, we have introduced a new quantity, dC_{g-V}, that is the gravimetric capacity (C_g) per volume expansion percentage (dV %), as derived below.

$$dV\% = [(V - V_{ref})/V_{ref}] \times 100 \qquad (1)$$

$$dC_{g-V} = C_g/dV \% \qquad (2)$$

where V is the volume of Li_nX, V_{ref} is the volume of starting X as the reference, and dV % is the percentage of volume expansion after lithiation. Obviously, a good anode material should have both a large C_g and a large dC_{g-V}, representing a high power density with a low volume expansion after lithiation. On the other hand, the formation energy ΔE_f (eV

per formula unit, f.u.) reflects the thermodynamics of lithiation with reference to the bulk Li metal and the bulk X, given by $\Delta E_f = E_{Li_nX} - nE_{Li} - E_X$, which can be further related to the open-circuit voltage V_0 via the Nernst equation, $V_0 = -\Delta E_f/nF$ (F: Faraday constant). For the ideal anode, V_0 should be positive but close to zero in order to yield the high output voltage. By using dC_{g-V} and ΔE_f as two key measures, we are able to fast screen anode candidates: the promising ones should appear on the top-right corner in the $dC_{g-V} \sim \Delta E_f$ plot.

By plotting dC_{g-V} against ΔE_f of the most stable LiX phases, Figure 1a shows that, interestingly, group IV$_A$ materials, C, Si,
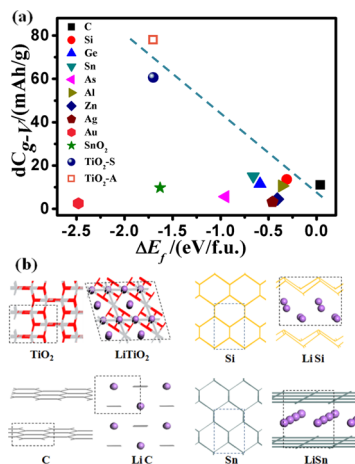

Figure 1. (a) dC_{g-V} vs ΔE_f plot for LiX materials (host phase X = C, Si, Ag, Al, As, Ge, Zn, Au, Sn, SnO$_2$, and TiO$_2$); (b) most stable structures for C, Si, Sn, and TiO$_2$ after lithiation together with the initial pure phases. Li: magenta balls; host phases: lines. Also see the Supporting Information for the structures of all other lithiated phases (Figure S1).

and Sn, outperform others at the low ΔE_f (−0.75 to 0 eV), while TiO$_2$ is the best at the medium ΔE_f region (∼−1.70 eV), as guided by the dotted line. The group IV materials such as C and Si have relatively large C_g than other materials, despite their large volume expansion. On the other hand, TiO$_2$ has a good C_g and a low volume expansion, which thus produces the far higher dC_{g-V} (61 and 78 mA h/g) than others.

To provide deeper insights into the $dC_{g-V} \sim \Delta E_f$ relation, we have analyzed in detail the structure after lithiation for these materials. In Figure 1b, we show the structures for the four representative materials C, Si, Sn, and TiO$_2$. The structures for others are detailed in the Supporting Information (Figure S1). In general, we note that these most stable LiX phases can be divided into three categories according to their structural features: (i) tunnel structures, as represented by TiO$_2$ (also in SnO$_2$, metals Ag, Au, Al, and Zn); (ii) layer structures, as represented by Si (also in Ge, Sn, and As); and (iii) solid–solution structure, as represented by C, where LiC is a mix of carbon dimers and Li atoms. From SSW global optimization, it is clear that the intercalation of Li atoms, driven by thermodynamics, tends to expand the volume of the host to fit into the new-coming Li, which leads to the solid phase transition from the dense structure of the host to the Li-intercalated open phases. In the following, we describe in detail the lithiated products for the four materials.

TiO$_2$: it is generally known that LiTiO$_2$ exists in various polymorphic modifications, such as anatase,[23,41] spinel,[29]

ramsdellite,[30,42] and orthorhombic.[43,44] Interestingly, the SSW method has determined two stable polymorphs for LiTiO$_2$ according to the thermodynamics: one in a spinel-like lattice of TiO$_2$ (TiO$_2$-S) and another in an anatase lattice (TiO$_2$-A). For the most stable LiTiO$_2$ (in the TiO$_2$-S lattice), it has a relatively low volume expansion after lithiation to LiTiO$_2$, dV % = 5.5%, thus achieving the high dC_{g-V} (61 mA h/g) even with a moderate C_g = 335.5 mA h/g. For the less stable LiTiO$_2$ (in the TiO$_2$-A lattice), the volume expansion is lower (4.3%), and thus, the dC_{g-V} has increased to 78 mA h/g. LiTiO$_2$ with the anatase lattice is slightly less stable than that with the TiO$_2$-S lattice, 0.66 meV per TiO$_2$ formula unit (f.u.). ΔE_f of them are relatively low, −1.70 eV, reflecting the large exothermicity of lithiation, which, on the other hand, implies the high stability of the lithiated product. For the structures with other TiO$_2$ lattices, for example, spinel, ramsdellite, and orthorhombic tunnel structures, their ΔE_f are relatively higher, above −1.59. The ΔE_f in LiTiO$_2$ suggests that TiO$_2$ has a relatively lower output voltage compared to C, Si, and Sn materials.

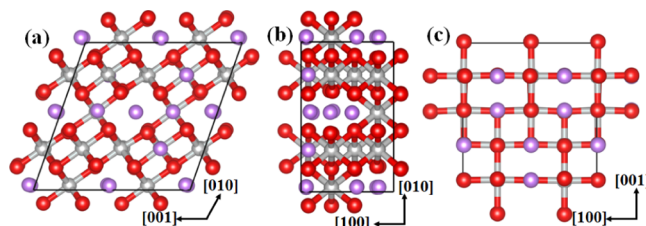The crystal structures for LiTiO$_2$ in TiO$_2$-S and TiO$_2$-A lattices are highlighted in Figure 2 from different view angles.

Figure 2. Ball-and-stick representations of TiO$_2$-S (a,b) and TiO$_2$-A (c) structures after lithiation (LiTiO$_2$) as identified from SSW−NN global search. Li atoms locate at the octahedral interstitial sites (Li−O bond ∼2.1 Å) in both lattices. O: red balls; Ti: gray balls; Li: magenta balls.

Both lattices are three-dimensional (3-D) interlinked structures with tunnels. The TiO$_2$-S crystal structure (space group $C2/C$) differs slightly from the common spinel structure in that a layer of TiO$_6$ octahedra per unit cell slips along [100] by half of the lattice length (as shown in Figure 2a,b and Supporting Information, Figure S2). It has a 3-D tunnel spinel-like crystal structure with a density of 3.82 g/cm^3, 2.8% lower than that of anatase. For LiTiO$_2$ in the TiO$_2$-A lattice, the optimized lattice constants are a, b = 4.08 Å, c = 8.48 Å, $\alpha = \beta = \gamma = 90°$ with the space group $I4_1/amd$. These structural data are consistent with the experimental measurement of anatase-type LiTiO$_2$ by neutron diffraction.[24]

We must emphasize that the energy difference between two LiTiO$_2$ (TiO$_2$-S and TiO$_2$-A lattices) is extremely small (0.66 meV per f.u.), suggesting that the thermodynamic-driven force to phase transition at the LiTiO$_2$ stage is not huge. This would help to maintain the structural integrity in Li intercalation–deintercalation cycles. In particular, the newly identified TiO$_2$-S may show excellent stability and cycling performance because it is the most stable structure at the high Li composition condition.

Si: ΔE_f for forming LiSi is −0.31 eV, suggesting that the Si anode has a good output voltage. Unfortunately, the volume expansion at the LiSi product is huge, dV % = 70.7%, which in turn reduces the dC_{g-V} despite its large C_g = 957.1 mA h/g. Importantly, as shown in Figure 1b, the Li addition destroys a

significant number of Si—Si bonds in the Si crystal (diamond) and leads to the formation of Si layer structures.

C: ΔE_f for forming LiC is positive, indicating that such a high Li composition is thermodynamically prohibited. This is consistent with the general knowledge on the limiting C_g of LiC_6 for graphite. The poor energetics can be attributed to the huge structural deformation. The LiC phase has the largest volume expansion percentage (dV % = 203.5%) among all materials. Only individual C—C dimers are present in the LiC phase and surrounded by intercalated Li atoms (Figure 1b).

Sn: the lithiation of Sn is similar to that of Si on many aspects. ΔE_f for forming LiSn is −0.66 eV, being 0.35 lower than that of Si. Because of the larger mass weight of Sn than that of Si, the capacity C_g is lower for Sn. However, the d$C_{g\text{-}V}$ is similar with that of Si, because its volume expansion is in fact much lower, dV % = 15.1%. The most stable LiSn phase is also a layer structure with Li filling in between Sn layers (Figure 1b).

From the above results, we reveal that the lithiation to high capacity will weaken dramatically the bondings of the host material and induce the solid phase transition toward open structures. This thermodynamic trend implies that the high capacity and the low volume expansion are a pair of paradoxical properties. To circumvent the problem, an obvious means is to abandon the common stable forms of the material but search for metastable new forms with stable open structures. The delithiated phases with open skeletons could be the more natural choices provided that they are stable enough in subsequent (dis)charging cycles.

3.2. Fine Screening. Along this line, we go further to select TiO_2 and Si for a fine screening, where their stepwise structural evolution during Li intercalation will be examined in detail. From Figure 1a, TiO_2 and Si are the materials most likely to achieve a balanced performance with high capacity density and good stability. We focus on the lithiated products of Si and TiO_2 at different stages of Li/X ratio, spanning from 0.5 to 3, including $Li_{0.5}TiO_2$, $LiTiO_2$, Li_2TiO_2, and Li_3TiO_2 for TiO_2 and $Li_{0.5}Si$, $Li_{0.75}Si$, LiSi, $Li_{1.25}Si$, $Li_{1.5}Si$, and Li_2Si for Si.

While DFT-based SSW PES exploration is utilized for structure search in Li_xSi systems, we combine the SSW method with the recently developed global NN potential to construct the global PES of Li_xTiO_2 and to assess their structural evolution, not least because of great structural complexity in ternary Li_xTiO_2 systems. Despite the added computational cost for the first-principles dataset generation, the SSW−NN method allows to fast obtain the global PES of Li_xTiO_2 because the NN simulation is at least 3−4 orders of magnitude faster than DFT (the accuracy of NN computation in energy and force is comparable with that from DFT, see the Supporting Information). In this work, each composition of Li_xTiO_2 is simulated in different unit cells from 12 to 64 atoms and explored to cover more than 10 000 minima on PES by SSW [the calculation detail and our benchmark between DFT and the NN potential for Li_xTiO_2 are shown in Supporting Information (Table S1)]. From the SSW−NN simulation, a large variety of Li_xTiO_2 structures ranging from crystalline to amorphous structures are obtained, from which the stable polymorphs are determined by further DFT validation. By analyzing the collected most stable structure for each composition (see geometrical structures in Supporting Information, Figures S3 and S4), we can see that with the gradual intercalation of Li to the electrode framework, the original network of the host is weakened and broken that

eventually results in the formation of small clusters of the host material surrounded by Li ions. The most stable structures of the TiO_2 electrode exhibit the spinel ($Li_{0.5}TiO_2$), TiO_2-S ($LiTiO_2$), and layer structures successively with the increase of Li intercalation. For the Si electrode, the crystalline−amorphous evolution can be clearly observed as the Li contents increase.[18,45,46] The structure evolution of Si follows the pattern from the diamond matrix ($Li_{0.5}Si$) to the sheets of the hexatomic ring (LiSi) and to a zigzag chain (Li_2Si).

Three major trends are found from the volume and energetics data of these Li intercalated phases. First, with the increase of Li/X ratio, the volume for both systems increases gradually, as shown by the volume versus Li/X ratio plot in Figure 3a. Interestingly, we found that the volume of TiO_2
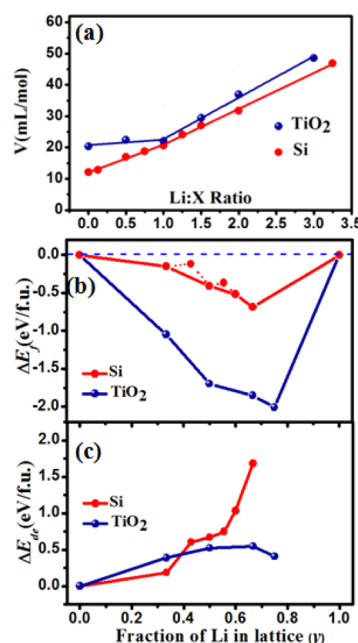
Figure 3. (a) Volume (mL/mol) of Si and TiO_2 after lithiation; (b) formation energy (ΔE_f) convex hull of Si and TiO_2 at varied Li fraction y ($Li_yX_{1−y}$); (c) stability (ΔE_{de}) for delithiated TiO_2 and Si phases at varied Li fraction.

increases however marginally at the initial stage of low Li/X ratios (≤1). We found that this is caused by the polymorphism of 3-D tunnel TiO_2 phases that are able to accommodate Li ions at the low concentrations. The 3-D tunnel structure can be created by reducing the O anion coordination as reflected by the appearance of two-coordinated O in the bulk (see Figure 2). The volume versus Li/X ratio curves at the large ratios becomes very similar, although Si and TiO_2 are very different in bonding nature. The slope of both linear lines is close to the density of the Li metal (13.0 mL/mol per Li atom). The volume for the predicted LiSi phase (20.6 mL/mol) is consistent with the experimental result at about the same ratio (~19 mL/mol),[47] which validates our theoretical prediction for the LiSi phases.

Second, the formation energy ΔE_f for both Si and TiO_2 lithiation exhibits the typical convex hull with the increase of Li fraction y in the lattice ($Li_yX_{1−y}$) as shown in Figure 3b. The largest ΔE_f occurs at the Li fraction of 0.5−0.8 for TiO_2 phases, while it is 0.6−0.7 for Si phases. They are the thermodynamically preferred phases after lithiation. The ΔE_f for the lithiation of TiO_2 is consistently larger than that of Si,

which can be explained by the strong ionic character of Li−O bonds that are present in the lithiated TiO_2.

Third, the delithiated structures for TiO_2 are generally more stable than those for Si, especially when the Li fraction is larger than 0.45 as shown in Figure 3c. The energy change after Li depletion ΔE_{de}(eV/f.u.) that measures the material stability after discharging is defined as $\Delta E_{de} = E_{X'} - E_X$, where $E_{X'}$ is the total energy from DFT for the skeleton X generated from Li_nX by relaxing Li-removed skeleton X while keeping the volume. The lower the ΔE_{de}, the more stable the delithiated phase will be. From Figure 3c, it can be seen that TiO_2 is particularly advantageous to achieve a high stability with high Li contents.

3.3. Property Assessment. Taking TiO_2 as the target material, we have finally investigated the (dis)charging kinetics for Li diffusion inside the TiO_2 tunnel. The migration paths for $LiTiO_2$-S/A and $Li_{0.5}TiO_2$-S/A have also been studied by creating one Li vacancy in the Li_xTiO_2 crystal and determining the lowest energy pathway for Li diffusion from the neighboring site to this vacancy.

As shown in Figure 4 (also in Supporting Information, Figure S5), we found that the Li diffusion barrier (E_a: 0.55 eV)
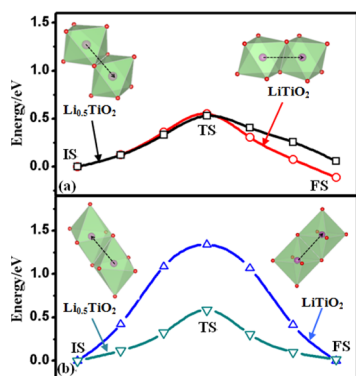

Figure 4. Lowest energy pathway of Li diffusion in (a) TiO_2-S and (b) TiO_2-A at different Li concentrations.

in the fully lithiated TiO_2-S structure ($LiTiO_2$) is not much different from the corresponding dilute $Li_{0.5}TiO_2$ (0.53 eV). This suggests that TiO_2-S would maintain the high rate even at high capacity. The presence of the 3-D tunnel in TiO_2-S plays the key role for the Li migration channel, which is critical for the purpose of fast charging. For the anatase crystal (TiO_2-A), however, the Li diffusion barrier increases noticeably from 0.59 to 1.34 eV with the increase of Li content from $Li_{0.5}TiO_2$ to $LiTiO_2$. This result is consistent with the previous calculations (~0.50 eV for $Li_{0.5}TiO_2$ and 1.37 eV for $LiTiO_2$)[48,49] and experimental measurement (~0.5−0.6 eV for $Li_{\sim0.5}TiO_2$[48,50]).

The difference in the barrier between pathways may be understood from the structure of the diffusion pathway. When Li diffuses out from one octahedral site, the two oxygen atoms of octahedral apexes have to be lengthened to allow Li to pass through. Because of the elongation of the O−O distance that weakens the original Ti−O bonding, it creates the barrier for Li diffusion. We found that the O−O distance increases by ~0.28 Å for the $LiTiO_2$-S structure and ~0.25 Å for $Li_{0.5}TiO_2$-S and $Li_{0.5}TiO_2$-A but much higher, ~0.4 Å (from 3.0 to 3.4 Å), for $LiTiO_2$-A during Li diffusion. This change in distance is in accordance with the computed diffusion barrier heights. For the $LiTiO_2$-S structure, we found that all Li-occupying octahedral sites are distorted because of the presence of the

3-D tunnel structure, where the O−O distance varies from 2.9 to 3.2 Å. However, in $LiTiO_2$-A, Li can distribute rather uniformly in the anatase skeleton with an O−O distance of 2.9−3.0 Å. The high barrier in $LiTiO_2$-A can thus be attributed to the small octahedral distortion as suggested previously.[49]

$$j = nFA \exp(-E_a/RT)/m_{(TiO_2)} \qquad (3)$$

From microkinetics, we can estimate the rate (j) of Li charging based on eq 3, where A is the pre-exponential factor (here, it is set as a typical value of 10^{12}), E_a is the diffusion barrier, and m is the mass weight of TiO_2. In $LiTiO_2$-S, the rate is estimated to be ~450 C, corresponding to ~8 s of charging/discharging. In contrast, the formation of the fully lithiated $LiTiO_2$-A is kinetically inhibited with a very low rate, ~10^{-11} C.

Experimentally, while nanoporous structures are known to improve the (dis)charging performance of lithium-ion batteries,[51,52] only recently the interconnected framework composed of ultrasmall spinel nanocrystals of a few nanometers in size ($Li_4Ti_5O_{12}$ spinel) has been synthesized and exhibits a high-rate performance of ~130 mA h/g at 800 C.[53] While the crystal $Li_4Ti_5O_{12}$ is not exactly the same with our predicted crystal $LiTiO_2$-S, the experiment evidence together with our results do suggest that the (spinel) tunnel crystal structure of TiO_2 can have the superior performance for the Li-ion battery, especially on the fast charging kinetics.

4. CONCLUSIONS

This work proposes a general strategy for high-throughput computational screening of the anode material based on the efficient global PES exploration. To demonstrate the approach, we select 11 different materials and study their structural evolution after lithiation. From the large dataset of lithiated phases, we find that the common carbon anode and silicon anode suffer from large C_g loss because of the massive volume expansion after lithiation, which is in fact intrinsic to most bulk materials. A new TiO_2 phase with a 3-D spinel-like tunnel structure that can in situ be produced during lithiation is discovered to be a high-performance anode material. The general rules for material structural deformation revealed here should be applicable for understanding the experimental findings and guiding the development of new anode materials.

■ ASSOCIATED CONTENT

ⓢ Supporting Information

The Supporting Information is available free of charge on the ACS Publications website at DOI: 10.1021/acs.jpcc.9b04604.

> SSW global structure search, SSW global PES exploration using NN potential, and DFT calculations; structure gallery of Li_xX phases; and Cartesian atomic coordinates of Li_xX phases (PDF)

■ AUTHOR INFORMATION

Corresponding Authors
*E-mail: yhfang@fudan.edu.cn (Y.-H.F.).
*E-mail: zpliu@fudan.edu.cn (Z.-P.L.).

ORCID ⓞ
Ya-Hui Fang: 0000-0001-5533-4962
Zhi-Pan Liu: 0000-0002-2906-5217

Notes
The authors declare no competing financial interest.

■ REFERENCES

(1) Tarascon, J.-M.; Armand, M. Issues and Challenges Facing Rechargeable Lithium Batteries. *Nature* **2001**, *414*, 359−367.

(2) Ren, Y.; Liu, Z.; Pourpoint, F.; Armstrong, A. R.; Grey, C. P.; Bruce, P. G. Nanoparticulate TiO$_2$(B): An Anode for Lithium-Ion Batteries. *Angew. Chem., Int. Ed.* **2012**, *51*, 2164−2167.

(3) Chockla, A. M.; Harris, J. T.; Akhavan, V. A.; Bogart, T. D.; Holmberg, V. C.; Steinhagen, C.; Mullins, C. B.; Stevenson, K. J.; Korgel, B. A. Silicon Nanowire Fabric as a Lithium Ion Battery Electrode Material. *J. Am. Chem. Soc.* **2011**, *133*, 20914−20921.

(4) Gentili, V.; Brutti, S.; Hardwick, L. J.; Armstrong, A. R.; Panero, S.; Bruce, P. G. Lithium Insertion into Anatase Nanotubes. *Chem. Mater.* **2012**, *24*, 4468−4476.

(5) Reddy, M. V.; Subba Rao, G. V.; Chowdari, B. V. R. Metal Oxides and Oxysalts as Anode Materials for Li Ion Batteries. *Chem. Rev.* **2013**, *113*, 5364−5457.

(6) Ma, S.; Huang, S.-D.; Fang, Y.-H.; Liu, Z.-P. Microporous Titania Crystals with Penta-Oxygen Coordination. *ACS Appl. Energy Mater.* **2018**, *1*, 22−26.

(7) Zaghib, K.; Song, X.; Guerfi, A.; Kostecki, R.; Kinoshita, K. Effect of Particle Morphology on Lithium Intercalation Rates in Natural Graphite. *J. Power Sources* **2003**, *124*, 505−512.

(8) Stokes, K.; Flynn, G.; Geaney, H.; Bree, G.; Ryan, K. M. Axial Si-Ge Heterostructure Nanowires as Lithium-Ion Battery Anodes. *Nano Lett.* **2018**, *18*, 5569−5575.

(9) Liu, D.; Liu, Z. J.; Li, X.; Xie, W.; Wang, Q.; Liu, Q.; Fu, Y.; He, D. Group IVA Element (Si, Ge, Sn)-Based Alloying/Dealloying Anodes as Negative Electrodes for Full-Cell Lithium-Ion Batteries. *Small* **2017**, *13*, 1702000.

(10) Park, M.-S.; Wang, G.-X.; Kang, Y.-M.; Wexler, D.; Dou, S.-X.; Liu, H.-K. Preparation and Electrochemical Properties of Sno$_2$ Nanowires for Application in Lithium-Ion Batteries. *Angew. Chem., Int. Ed.* **2007**, *46*, 750−753.

(11) Lai, C.; Li, G. R.; Dou, Y. Y.; Gao, X. P. Mesoporous Polyaniline or Polypyrrole/Anatase TiO$_2$ Nanocomposite as Anode Materials for Lithium-Ion Batteries. *Electrochim. Acta* **2010**, *55*, 4567−4572.

(12) Beaulieu, L. Y.; Eberman, K. W.; Turner, R. L.; Krause, L. J.; Dahn, J. R. Colossal Reversible Volume Changes in Lithium Alloys. *Electrochem. Solid-State Lett.* **2001**, *4*, A137−A140.

(13) Ryu, J. H.; Kim, J. W.; Sung, Y.-E.; Oh, S. M. Failure Modes of Silicon Powder Negative Electrode in Lithium Secondary Batteries. *Electrochem. Solid-State Lett.* **2004**, *7*, A306−A309.

(14) Obrovac, M. N.; Christensen, L. Structural Changes in Silicon Anodes During Lithium Insertion/Extraction. *Electrochem. Solid-State Lett.* **2004**, *7*, A93−A96.

(15) Patil, A.; Patil, V.; Wook Shin, D.; Choi, J.-W.; Paik, D.-S.; Yoon, S.-J. Issue and Challenges Facing Rechargeable Thin Film Lithium Batteries. *Mater. Res. Bull.* **2008**, *43*, 1913−1942.

(16) Li, H.; Huang, X.; Chen, L.; Zhou, G.; Zhang, Z.; Yu, D.; Jun Mo, Y.; Pei, N. The Crystal Structural Evolution of Nano-Si Anode Caused by Lithium Insertion and Extraction at Room Temperature. *Solid State Ionics* **2000**, *135*, 181−191.

(17) Limthongkul, P.; Jang, Y.-I.; Dudney, N. J.; Chiang, Y.-M. Electrochemically-Driven Solid-State Amorphization in Lithium-Silicon Alloys and Implications for Lithium Storage. *Acta Mater.* **2003**, *51*, 1103−1113.

(18) Chan, M. K. Y.; Wolverton, C.; Greeley, J. P. First Principles Simulations of the Electrochemical Lithiation and Delithiation of Faceted Crystalline Silicon. *J. Am. Chem. Soc.* **2012**, *134*, 14362−14374.

(19) Johari, P.; Qi, Y.; Shenoy, V. B. The Mixing Mechanism During Lithiation of Si Negative Electrode in Li-Ion Batteries: An Ab Initio Molecular Dynamics Study. *Nano Lett.* **2011**, *11*, 5494−5500.

(20) Stashans, A.; Lunell, S.; Bergström, R.; Hagfeldt, A.; Lindquist, S.-E. Theoretical Study of Lithium Intercalation in Rutile and Anatase. *Phys. Rev. B: Condens. Matter Mater. Phys.* **1996**, *53*, 159−170.

(21) Kerisit, S.; Rosso, K. M.; Yang, Z.; Liu, J. Computer Simulation of the Phase Stabilities of Lithiated TiO$_2$ Polymorphs. *J. Phys. Chem. C* **2010**, *114*, 19096−19107.

(22) Fröeschl, T.; Höermann, U.; Kubiak, P.; Kucerova, G.; Pfanzelt, M.; Weiss, C. K.; Behm, R. J.; Huesing, N.; Kaiser, U.; Landfester, K.; Wohlfahrt-Mehrens, M. High Surface Area Crystalline Titanium Dioxide: Potential and Limits in Electrochemical Energy Storage and Catalysis. *Chem. Soc. Rev.* **2012**, *41*, 5313−5360.

(23) Borghols, W. J. H.; Lützenkirchen-Hecht, D.; Haake, U.; van Eck, E. R. H.; Mulder, F. M.; Wagemaker, M. The Electronic Structure and Ionic Diffusion of Nanoscale LiTiO$_2$ Anatase. *Phys.Chem.Chem.Phys.* **2009**, *11*, 5742−5748.

(24) Wagemaker, M.; Borghols, W. J. H.; Mulder, F. M. Large Impact of Particle Size on Insertion Reactions. A Case for Anatase Li$_x$TiO$_2$. *J. Am. Chem. Soc.* **2007**, *129*, 4323−4327.

(25) Saravanan, K.; Ananthanarayanan, K.; Balaya, P. Mesoporous TiO$_2$ with High Packing Density for Superior Lithium Storage. *Energy Environ. Sci.* **2010**, *3*, 939−948.

(26) Fattakhova-Rohlfing, D.; Wark, M.; Brezesinski, T.; Smarsly, B. M.; Rathouský, J. Highly Organized Mesoporous TiO$_2$ Films with Controlled Crystallinity: A Li-Insertion Study. *Adv. Funct. Mater.* **2007**, *17*, 123−132.

(27) Belak, A. A.; Wang, Y.; Van der Ven, A. Kinetics of Anatase Electrodes: The Role of Ordering, Anisotropy, and Shape Memory Effects. *Chem. Mater.* **2012**, *24*, 2894−2898.

(28) Kang, J. W.; Kim, D. H.; Mathew, V.; Lim, J. S.; Gim, J. H.; Kim, J. Particle Size Effect of Anatase TiO2 Nanocrystals for Lithium-Ion Batteries. *J. Electrochem. Soc.* **2011**, *158*, A59−A62.

(29) Cava, R. J.; Murphy, D. W.; Zahurak, S.; Santoro, A.; Roth, R. S. The Crystal-Structures of the Lithium-Inserted Metal-Oxides Li0.5TiO2 Anatase, LiTi2O4 Spinel, and Li2ti2o4. *J. Solid State Chem.* **1984**, *53*, 64−75.

(30) Kuhn, A.; Baehtz, C.; García-Alvarado, F. Structural Evolution of Ramsdellite-Type Lixti2o4 Upon Electrochemical Lithium Insertion-Deinsertion (0 < = X < = 2). *J. Power Sources* **2007**, *174*, 421−427.

(31) Shang, C.; Liu, Z.-P. Stochastic Surface Walking Method for Structure Prediction and Pathway Searching. *J. Chem. Theory Comput.* **2013**, *9*, 1838−1845.

(32) Zhang, X.-J.; Shang, C.; Liu, Z.-P. From Atoms to Fullerene: Stochastic Surface Walking Solution for Automated Structure Prediction of Complex Material. *J. Chem. Theory Comput.* **2013**, *9*, 3252−3260.

(33) Zhu, S.-C.; Xie, S.-H.; Liu, Z.-P. Nature of Rutile Nuclei in Anatase-to-Rutile Phase Transition. *J. Am. Chem. Soc.* **2015**, *137*, 11532−11539.

(34) Guan, S.-H.; Zhang, X.-J.; Liu, Z.-P. Energy Landscape of Zirconia Phase Transitions. *J. Am. Chem. Soc.* **2015**, *137*, 8010−8013.

(35) Li, Y.-F.; Zhu, S.-C.; Liu, Z.-P. Reaction Network of Layer-to-Tunnel Transition of Mno2. *J. Am. Chem. Soc.* **2016**, *138*, 5371−5379.

(36) Huang, S.-D.; Shang, C.; Zhang, X.-J.; Liu, Z.-P. Material Discovery by Combining Stochastic Surface Walking Global Optimization with a Neural Network. *Chem. Sci.* **2017**, *8*, 6327−6337.

(37) Ma, S.; Huang, S.-D.; Fang, Y.-H.; Liu, Z.-P. Tih Hydride Formed on Amorphous Black Titania: Unprecedented Active Species for Photocatalytic Hydrogen Evolution. *ACS Catal.* **2018**, *8*, 9711−9721.

(38) Shang, C.; Huang, S.-D.; Liu, Z.-P. Massively Parallelization Strategy for Material Simulation Using High-Dimensional Neural Network Potential. *J. Comput. Chem.* **2019**, *40*, 1091−1096.

(39) Huang, S.-D.; Shang, C.; Kang, P.-L.; Zhang, X.-J.; Liu, Z.-P. Lasp: Fast Global Potential Energy Surface Exploration. *Wiley Interdiscip. Rev.: Comput. Mol. Sci.* **2019**, No. e1415.

(40) Ma, S.; Huang, S.-D.; Liu, Z.-P. Dynamic Coordination of Cations and Catalytic Selectivity on Zinc−Chromium Oxide Alloys During Syngas Conversion. *Nat. Catal.* **2019**, DOI: 10.1038/s41929-019-0293-8.

(41) Bhatt, M. D.; O'Dwyer, C. Recent Progress in Theoretical and Computational Investigations of Li-Ion Battery Materials and Electrolytes. *Phys.Chem.Chem.Phys.* **2015**, *17*, 4799−4844.

(42) Akimoto, J.; Gotoh, Y.; Oosawa, Y.; Nonose, N.; Kumagai, T.; Aoki, K.; Takei, H. Topotactic Oxidation of Ramsdellite-Type Li0.5TiO2, a New Polymorph of Titanium-Dioxide-TiO2(R). *J. Solid State Chem.* **1994**, *113*, 27−36.

(43) Murphy, D.; Cava, R.; Zahurak, S.; Santoro, A. Ternary Li_xTiO_2 Phases from Insertion Reactions. *Solid State Ionics* **1983**, *9−10*, 413−417.

(44) Liu, H.; Grey, C. P. Influence of Particle Size, Cycling Rate and Temperature on the Lithiation Process of Anatase TiO_2. *J. Mater. Chem. A* **2016**, *4*, 6433−6446.

(45) Key, B.; Morcrette, M.; Tarascon, J.-M.; Grey, C. P. Pair Distribution Function Analysis and Solid State Nmr Studies of Silicon Electrodes for Lithium Ion Batteries: Understanding the (De)-Lithiation Mechanisms. *J. Am. Chem. Soc.* **2011**, *133*, 503−512.

(46) Key, B.; Bhattacharyya, R.; Morcrette, M.; Seznéc, V.; Tarascon, J.-M.; Grey, C. P. Real-Time Nmr Investigations of Structural Changes in Silicon Electrodes for Lithium-Ion Batteries. *J. Am. Chem. Soc.* **2009**, *131*, 9239−9249.

(47) Obrovac, M. N.; Christensen, L.; Le, D. B.; Dahn, J. R. Alloy Design for Lithium-Ion Battery Anodes. *J. Electrochem. Soc.* **2007**, *154*, A849−A855.

(48) Lunell, S.; Stashans, A.; Ojamäe, L.; Lindström, H.; Hagfeldt, A. Li and Na Diffusion in TiO2 from Quantum Chemical Theory Versus Electrochemical Experiment. *J. Am. Chem. Soc.* **1997**, *119*, 7374−7380.

(49) Belak, A. A.; Wang, Y.; Van der Ven, A. Kinetics of Anatase Electrodes: The Role of Ordering, Anisotropy, and Shape Memory Effects. *Chem. Mater.* **2012**, *24*, 2894−2898.

(50) Lindström, H.; Södergren, S.; Solbrand, A.; Rensmo, H.; Hjelm, J.; Hagfeldt, A.; Lindquist, S.-E. Li^+ Ion Insertion in TiO2 (Anatase) .2. Voltammetry on Nanoporous Films. *J. Phys. Chem. B* **1997**, *101*, 7717−7722.

(51) Liu, H.; Bi, Z.; Sun, X.-G.; Unocic, R. R.; Paranthaman, M. P.; Dai, S.; Brown, G. M. Mesoporous TiO2-B Microspheres with Superior Rate Performance for Lithium Ion Batteries. *Adv. Mater.* **2011**, *23*, 3450−3454.

(52) Kim, S.-W.; Han, T. H.; Kim, J.; Gwon, H.; Moon, H.-S.; Kang, S.-W.; Kim, S. O.; Kang, K. Fabrication and Electrochemical Characterization of TiO2 Three-Dimensional Nanonetwork Based on Peptide Assembly. *ACS Nano* **2009**, *3*, 1085−1090.

(53) Feckl, J. M.; Fominykh, K.; Döblinger, M.; Fattakhova-Rohlfing, D.; Bein, T. Nanoscale Porous Framework of Lithium Titanate for Ultrafast Lithium Insertion. *Angew. Chem., Int. Ed.* **2012**, *51*, 7459−7463.